Carbohydrate Polymers 152 (2016) 832–840

Contents lists available at ScienceDirect

Carbohydrate Polymers

journal homepage: www.elsevier.com/locate/carbpol

Chitosan-chitin nanocrystal composite scaffolds for tissue engineering

Mingxian Liu [a,*], Huanjun Zheng [a], Juan Chen [a], Shuangli Li [a], Jianfang Huang [b], Changren Zhou [a,*]

[a] Department of Materials Science and Engineering, Jinan University, Guangzhou 510632, China
[b] Guangdong Province Key Laboratory of Molecular Immunology and Antibody Engineering, Jinan University, Guangzhou 510632, China

ARTICLE INFO

Article history:
Received 30 April 2016
Received in revised form 2 July 2016
Accepted 12 July 2016
Available online 14 July 2016

Keywords:
Chitosan
Chitin nanocrystal
Scaffold
Compressive property
Biocompatibility

ABSTRACT

Chitin nanocrystals (CNCs) with length and width of 300 and 20 nm were uniformly dispersed in chitosan (CS) solution. The CS/CNCs composite scaffolds prepared utilizing a dispersion-based freeze dry approach exhibit significant enhancement in compressive strength and modulus compared with pure CS scaffold both in dry and wet state. A well-interconnected porous structure with size in the range of 100–200 μm and over 80% porosity are found in the composite scaffolds. The crystal structure of CNCs is retained in the composite scaffolds. The incorporation of CNCs leads to increase in the scaffold density and decrease in the water swelling ratio. Moreover, the composite scaffolds are successfully applied as scaffolds for MC3T3-E1 osteoblast cells, showing their excellent biocompatibility and low cytotoxicity. The results of fluorescent micrographs images reveal that CNCs can markedly promote the cell adhesion and proliferation of the osteoblast on CS. The biocompatible composite scaffolds with enhanced mechanical properties have potential application in bone tissue engineering.

1. Introduction

Exploring high strength and low density porous scaffolds is one of the hot topics in the materials research areas, since these scaffolds have important applications in dye absorption, oil/water separation, heat insulating material, and tissue engineering. For obtaining the porous scaffolds, freeze-drying of corresponding solutions is an effective route. During this process, the ultra-low density of the materials is produced by replacement of solvent with air. The polymer porous scaffolds typically exhibit bulk densities of 0.1 g/cm^3 or lower. However, these polymer porous scaffolds with ultra-low density exhibit generally poor mechanical properties. For example, the pure chitosan (CS) porous scaffolds have greatly reduced elastic moduli (0.1–0.5 MPa) and compressive strength (~10 kPa) compared to non-porous CS membranes (Suh & Matthew, 2000). Previous study showed that the human compact bone has a compressive strength of 220 MPa with a density of 1.8 g/cm^3 (Carter & Hayes, 1976). The poor mechanical properties limit their practical applications in tissue engineering. The incorporation of nanoparticles with high aspect ratios into these structures can greatly increase their strengths and moduli. Carbon nanotube (Lau, Cooney & Atanassov, 2008; Sweetman, Moulton & Wallace, 2008), graphene (Fan et al., 2010; Justin & Chen, 2014), clays (Liu, Wu, Jiao, Xiong & Zhou, 2013; Tang et al., 2008; Wang, Du, Luo, Lin & Kennedy, 2007), and cellulose nanowhisker (de Mesquita, Donnici & Pereira, 2010; Li, Zhou & Zhang, 2009) were added into the CS scaffolds to improve the mechanical properties. The nanofibers from chitin and CS prepared with electrospinning, self-assembly, phase separation, mechanical treatment, printing, ultrasonication and chemical treatment also have tremendous potential to be used as drug delivery systems, tissue engineering scaffolds, wound dressing materials, antimicrobial agents, and biosensors (Ding, Deng, Du, Shi & Wang, 2014).

Chitin nanocrystals (CNCs), a novel type of nanoparticles from biological source, can be used to reinforce the polymer scaffolds (Lin, Huang & Dufresne, 2012). CNCs, prepared via acidolysis of chitin, have a fiber or rod-like morphology with length and width of 300 and 20 nm. The high aspect ratio (~15) and high longitudinal modulus (150 GPa) of CNCs ensures them a high reinforcing effect on different polymers (Gopalan Nair & Dufresne, 2003; Huang, Zhang, Yang, Zhang & Xu, 2013; Liu, Peng, Luo & Zhou, 2015; Sriupayo, Supaphol, Blackwell & Rujiravanit, 2005a; Sriupayo, Supaphol, Blackwell & Rujiravanit, 2005b; Wongpanit et al., 2007). CNCs can interact with the matrix via hydrogen bonding interactions, which further improve the structural and biological properties (Liu, Huang, Luo & Zhou, 2015; Liu, Peng et al., 2015). In addition, the good biosafety of the CNCs make them good candidate as nanoreinforcement for biomaterials. For

* Corresponding authors.
E-mail addresses: liumx@jnu.edu.cn (M. Liu), tcrz9@jnu.edu.cn (C. Zhou).

http://dx.doi.org/10.1016/j.carbpol.2016.07.042
0144-8617/

example, the incorporation of CNCs into the silk fibroin matrix was found to enhance the compression strength and promote cell spreading (Wongpanit et al., 2007). Alginate/CNCs nanocomposite hydrogels also showed improved mechanical properties and good cytocompatibility. The composite hydrogel has potential applications in bone tissue engineering (Huang et al., 2015). For designing the composite systems, the dispersion technology and the interfacial interactions between the CNCs and the matrix are critical. Due to similar molecular structure, CS and CNCs have good interfacial compatibility. Therefore, the CS/CNCs composites are expected to show improved properties. However, to the best of our knowledge, no such material of 3D porous scaffolds composed with CS and CNCs has been found to date.

In the present work, nanocomposite scaffolds composed of CNCs and CS were successfully fabricated. The effects of CNCs on the mechanical, thermal, crystal structure, and swelling behavior of CS scaffolds were studied. Furthermore, the promoted adhesion and proliferation of osteoblast by addition of CNCs were investigated and evaluated. These composite scaffolds have potential applications in bone tissue engineering.

2. Experimental

2.1. Materials

Chitosan (CS) was supplied by Jinan Haidebei Marine Bioengineering Co. Ltd, China. The deacetylation and viscosity-average molecular weight were 95% and 600,000 g/mol respectively. Chitin powder (C104157) was purchased from Aladdin Industrial Corporation, China and used without further purification. The degree of acetylation (DA) of the chitin was 0.98%. The chitin nanocrystals (CNCs) were prepared from chitin by acid hydrolysis according to the previous study (Gopalan Nair & Dufresne, 2003; Liu, Peng et al., 2015). The DA change of chitin before and after acid hydrolysis was checked by solid state ^{13}C NMR (Fig. S1). All the peaks in the two spectra appeared at same location and with same intensity. So, the DA of chitin did not change during the acid hydrolysis. The morphology of CNCs was observed with a ZEISS, Ultra55 SEM machine, Philips Tecnai 10 transmission electron microscopy (TEM) machine, and a multimode AFM with NanoScope IIIa controller (Veeco Instruments). The sample for SEM and AFM analysis was prepared by dropping of the 0.01 wt.% CNCs dispersion on clean mica plate and dried at room temperature. The particle size distribution and Zeta-potential of CNCs aqueous dispersion (0.01 wt.%) was measured with a Zetasizer Nano ZS (Malvern Ltd., UK). Other chemicals used in this study were of analytical grade and used as received. Water was purified by deionization and filtration with a Millipore purification apparatus (resistivity > 18.2 MΩ.cm).

2.2. Fabrication of CS/CNCs composite scaffolds

Solution-mixing and subsequent freeze-drying methods were used to prepare CS/CNCs composite scaffolds. Firstly, CNCs were dispersed in water by ultrasonic treatment using JY99-IIDN ultrasonic cell disruptor (NingBo Scientz Biotechnology Co., Ltd) at 800 W for 1 h. 2 wt.% CS acetic acid solution was subsequently mixed with the CNCs dispersion. The mixture dispersion was continuously stirred over 24 h in order to obtain the uniform dispersion. The cylinder samples were obtained by pouring the mixture into 24 well cell culture plate and subsequently freeze-dried at −80 °C using Christ freeze dryer ALPHA 1-2/LD plus. In order to neutralize the residual acid in the samples, the scaffolds were immersed in 2 wt.% NaOH solution, washed with deionized water, and freeze-dried again. The content of CNCs in the composite varied from 20% to 200% relative to the CS weight. Pure CS scaffold was also prepared in the same way but without addition of CNCs for comparison. CNCs alone can not form porous scaffold via the freeze-drying method, and the appearance of freeze-dried CNCs just like a pile of powder. So, we did not use the CNCs as the control group in the following experiment. The samples were kept in electronic moistureproof box before any measurement.

2.3. Characterization of CS/CNCs composite scaffolds

2.3.1. Fourier transform infrared spectroscopy (FTIR)

The FTIR spectra of CNCs powder, pure CS, and CS/CNCs composites (weight ratio is 1:1) were measured in a NICOLET iS10 FT-IR Spectrometer. Thirty-two consecutive scans were taken and their average was stored. Spectra were taken from 4000 to 400 cm^{-1}. The resolution of the wavenumber was 2 cm^{-1}.

2.3.2. Mechanical properties determinations

The compression property of the scaffolds was measured on an universal testing machine (Zwick/Roell Z005, Germany) under 25 °C according to ASTM D5024-95a at a speed of 2 mm/min. Compressive modulus was calculated as the slop of the initial linear portion of the stress-strain curves. The samples in wet state were also tested by the same procedure. Before measurement, the samples were soaked in PBS solution at 37 °C for 24 h. To investigate the elasticity of the samples, the deformation recovery ratio (R) was calculated by the following equation,

$$R(\%) = \frac{h_f - (1-\varepsilon)h_0}{\varepsilon h_0} \times \%$$

where, h_f was the final height of sample after 30 min of the compressive testing; h_0 was the initial height of the samples before compressive testing; ε was the deformation ratio when stopping the compression test (ε = 85% for the present work). For each sample, at least five parallel experiments were conducted and an average data and standard error was reported.

2.3.3. Scanning electron microscopy (SEM)

Scanning electron microscopy (SEM) was carried out on a field emission scanning electron microscopy Zeiss Ultra 55 SEM machine at 5 kV. Before observation, the fracture sections were sputtered with 10 nm thick gold–palladium.

2.3.4. Stereoscopic microscope

The microstructure of the cross section of the scaffolds was analyzed using ZEISS SteREO Discovery.V20, Germany. The photographs were taken at different depths approaching ~1000 μm along the z-axis.

2.3.5. X-Ray diffraction (XRD)

XRD measurement was carried out on a wide-angle X-ray diffraction (WXRD) diffractometer (D8-Advance, Bruker, U.S.A.) with Cu Kα radiation (λ = 0.154 nm). The scanning angle was from 5° to 50° at a scanning speed of 2°/min. The XRD patterns were recorded in the range 2θ = 5–50°.

2.3.6. Porosity measurement

The porosity of the porous scaffold sample was determined according to the method suggested in previous study (Zhang and Zhang, 2001). Typically, the scaffolds were immersed in absolute ethanol for 24 h and then weighed. Porosity was calculated using the equation,

$$\text{porosity} = \frac{W_2 - W_1}{\rho V_1} \times 100\%$$

where, W_1 and W_2 was the weight of scaffold before and after immersion in alcohol, respectively. V_1 was the volume before

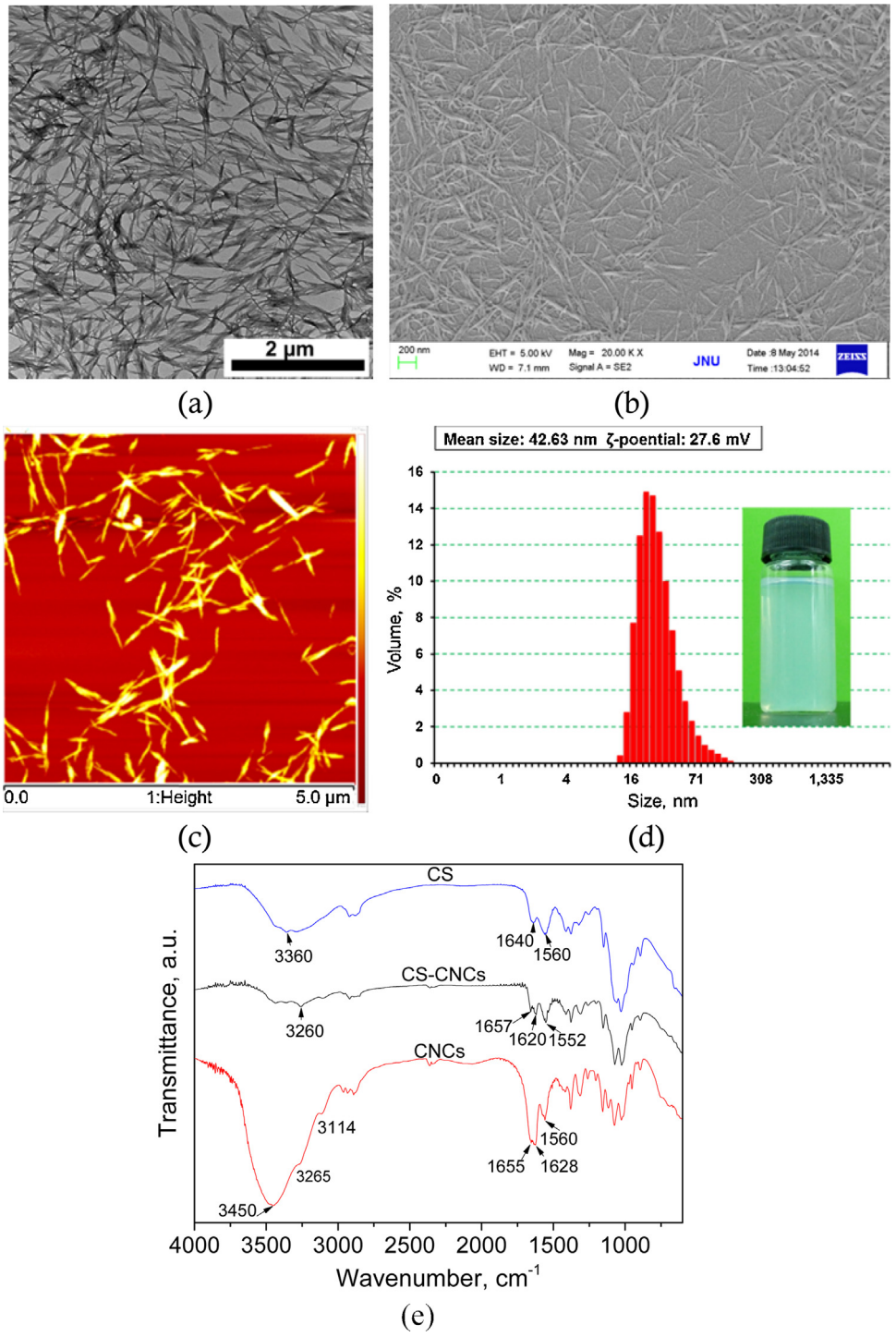

Fig. 1. TEM (a), SEM (b), AFM height-phase (c), and particle size distribution (d) of CNCs; FTIR of CS, CNCs, and CS/CNCs (weight ratio = 1:1) (e). The inset in (d) is the photo of CNCs aqueous dispersion. FTIR spectra of the CNCs, pure CS, and CS/CNCs scaffolds (weight ratio, 1:1) (e).

immersion in alcohol; ρ was the density of alcohol. Three parallel sets were analyzed for every scaffold and the mean value of the porosities of different scaffolds was taken.

2.3.7. Water uptake abilities

The water uptake ability (E_A) of scaffold was studied using the following procedure. Dry scaffolds were weighed (W_{dry}) and immersed in distilled water for 48 h. Then the scaffolds were gently removed from the beaker and placed on a wire mesh rack. Excess water was drained and scaffolds were weighed (W_{wet}) to determine water uptake. For each sample, at least five parallel experiments were conducted and an average data and standard error was reported.

$$E_A = \frac{W_{wet} - W_{dry}}{W_{dry}} \times 100\%$$

2.4. Cell adhesion and proliferation on pure CS and CS/CNCs composites

The pure CS scaffolds and CS/CNCs composite scaffolds were sectioned into 1 mm thick slice and then sterilized by exposure to

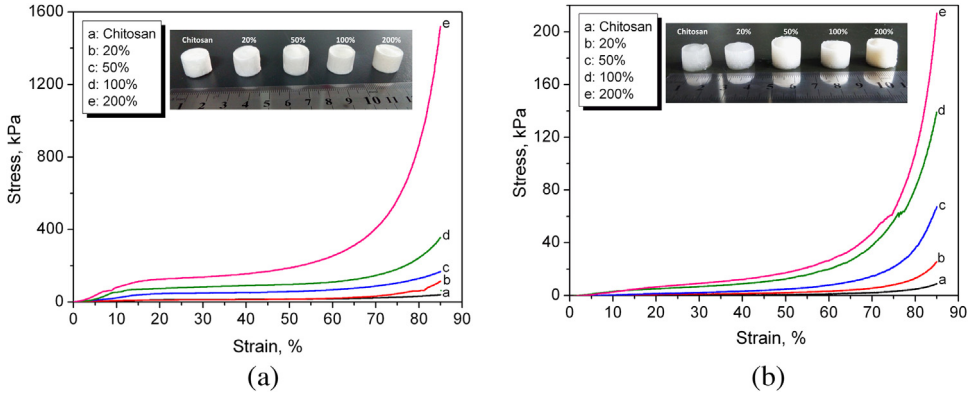

Fig. 2. Compressive stress-strain curves of CS/CNCs composite scaffolds in dry (a) and wet (b) state.

UV light for 30 min and soaked in the 0.1 mg/mL physiological saline for 0.5 h. MC3T3-E1 osteoblast cells were cultured in were cultured in α-minimal essential medium (α-MEM, Gibco, Life Technologies, Carlsbad, U.S.A.) with 10% fetal bovine serum, containing 100 U/mL penicillin and 100 mg/mL streptomycin in an incubator with 5.0% CO_2 at 37 °C. The cells were passaged every 2 days and the medium was changed every 3 days.

The viablity of MC3T3-E1 cells on different materials was characterized by using CCK-8 assay (KeyGEN BioTECH, China). Cells were seeded onto the substrates at a density of 4×10^4 cells/mL. At the time point of 1, 3, 5 days, CCK-8 solution was added to each well and incubated for 3 h at 37 °C. The absorbance was measured spectrophotometrically with a microplate reader (Bio-Rad, Model 680, USA) at wavelengths of 450 nm. Control was the absorbance of the cells incubated on TCPS only (positive control). Four parallel sets were analyzed for every group. All data were expressed as the mean ± standard deviation (SD) for $n = 4$.

The cell morphology was observed after 3 days culture. Cells were rinsed carefully with 37◦C phosphate buffer solution (PBS) to remove non-adherent cells. Then the cells were fixed with 4% paraformaldehyde in PBS for 30 min and then permeabilized with a 0.1% v/v Triton X-100 for 5 min. The cells were then incubated with 1 mg/mL Phalloidin-TRITC (Sigma) for 1 h at room temperature for labeling the filamentous actins. The nuclei were stained with 5 mg/mL 4′,6-diamidino-2-phenylindole (DAPI, Sigma) for 15 min. The stained samples were rinsed extensively with PBS, prior to observation under an immunofluorescence microscope (XDY-2, Yuexian, China).

3. Results and discussion

3.1. Characterization of CNCs and their interactions with CS

CNCs prepared by acid hydrolysis and ultrasonic treatment exhibit nanosized structure with high aspect ratio, which is confirmed by TEM, SEM, and AFM (Fig. 1(a)-(c)). CNCs can be completely exfoliated into nanofibers. CNCs have a rod-like morphology with average width of 15 nm, length of 200–500 nm, and aspect ratio of 13–33. The dynamic light scattering (DLS) result shows that CNCs ranges from 12.2 to 147.7 nm with mean diameter of 42.63 nm (Fig. 1(d)). CNCs aqueous dispersion has good stability without sedimentation for several months, which may due to the high Zeta-potential (+27.6 mV) and small dimension of CNCs. The high aspect ratio and good dispersion state in water of CNCs endow the promising applications in water soluble polymer nanocomposites.

To illustrate the possible interfacial interactions between CNCs and chitosan, FTIR spectra were measured for the CNCs, pure CS, and CS-CNCs scaffolds (weight ratio, 1:1) (Fig. 1(e)). Pure CS show characteristic bands at approximately 3450, 1560–1660 cm^{-1} corresponding to a region of amino and amide groups vibrations and at 1040–1150 cm^{-1} for —C—O—C— groups vibration (Pawlak & Mucha, 2003). CNCs shows peak around 3450 cm^{-1} (hydrogen-bonded OH groups), 3264 cm^{-1} (N—H groups), and 1628 cm^{-1} (C═O groups hydrogen-bonded OH groups), which are consistent with the spectrum of previous reported one (Lu et al., 2013). From the spectra of CS/CNCs, the N—H groups (3265 cm^{-1}), amide-I (1655 cm^{-1} and 1628 cm^{-1}) and amide-II (1560 cm^{-1}) bands of CNCs shift to 3260 cm^{-1}, 1657 cm^{-1}, 1620 cm^{-1}, and 1552 cm^{-1}, respectively. This suggests the interfacial hydrogen bonding between the hydroxyl and amide groups of chitin and CS.

3.2. Mechanical properties of the CS/CNCs composite scaffolds

As discussed above, CNCs exhibited a rod-like structure and can be uniformly dispersed in aqueous solution, which is important for the stress transfer in polymer composites. The effect of CNCs on the compressive properties of the CS scaffolds both in dry and wet state was investigated. Fig. 2(a) inset shows the appearance of the prepared scaffolds. The color, shape, porosity of the CS scaffolds CNCs is slightly different by the addition of CNCs. CNCs can improve the dimensional stability of the CS scaffold. By touching them by hand, an obvious stiffening of the composite scaffolds is found compared with the mechanically weak pure CS scaffolds. The compressive stress–strain curves for each group are shown in Fig. 2(a). The mechanical properties data is summarized in Table 1. It

Table 1
Summary of the mechanical properties of the CS/CNCs composite scaffolds in dry and wet state.

Sample	Elastic modulus in dry state (kPa)	Maximum load in dry state (N)	Elastic modulus in wet state (kPa)	Maximum load in wet state (N)	Deformation recovery ratio (%)
Chitosan	77.57 (2.11)	15.30 (0.63)	2.81 (0.40)	3.22 (1.70)	91.46 (2.70)
20%	82.47 (3.23)	17.15 (0.86)	4.79 (0.72)	6.02 (3.48)	90.96 (4.27)
50%	256.4 (5.24)	47.87 (1.03)	11.35 (1.75)	14.87 (8.65)	91.79 (2.18)
100%	356.9 (7.52)	50.47 (1.23)	31.90 (1.58)	32.43 (9.44)	87.42 (9.17)
200%	747.0 (10.23)	163.2 (3.26)	39.98 (6.25)	73.67 (1.23)	58.37 (10.46)

is clear that the composite scaffolds are stronger than pure CS scaffold. The curve of the composite scaffold is far above that of the pure CS scaffolds. The stress of the composite scaffold samples increase with the loading of CNCs. For instance, the compressive strength of the CS/CNCs composite scaffolds with 200% CNCs loading at 20%, 40%, and 60% strain increases by factors of 10, 11, and 14 respectively in comparison to pure CS scaffold. From the initial stage of the stress-stain curves, the compressive modulus can be calculated. Form Table 1, the compressive modulus of the composite scaffolds is also higher than that of pure CS scaffold. The maximum compressive modulus of the composite is 747.0 kPa, which is obtained at the 200% CNCs loading. Therefore, CNCs can effectively reinforce the CS scaffolds, which can be attributed to the high modulus of the CNCs and the formation of filler network in the composite (Capadona, Shanmuganathan, Tyler, Rowan & Weder, 2008; Liu, Peng et al., 2015). Also, the increased density and decreased porosity of the composite scaffold by the addition of CNCs also contribute to the increase in mechanical properties, which will be discussed in the following sections.

When implanted in body, the scaffolds are in wet state due to the contacting of body fluid. So, it is important to investigate the influence of CNCs on the mechanical properties of the scaffolds in wet state. The compressive properties of the scaffolds in wet state were tested by after soaking the scaffolds in PBS solution at 37 °C for 24 h. Fig. 2(b) shows the typical stress-strain curve for the samples in wet state. It can be seen that the mechanical properties for both the pure CS and the composite scaffolds are dramatically decreased in the wet state. The compressive modulus and the stress of the CS scaffold significantly increase by the addition of CNCs. For example, the CS/CNCs composites scaffolds with 200% CNCs loading shows elastic modulus, the stress at 40% strain, and the stress at 60% strain of 39.98 kPa, 12.2 kPa, and 26.5 kPa, which is 14.2, 36.9, and 21.7 folds than those of the pure CS scaffold respectively. It is concluded that the CS/CNCs composite scaffolds can tolerate much higher loading both in dry state and wet state. The improved strength of the scaffold is benefit for their applications in tissue engineering, as the scaffolds should act as temporary physical support to withstand the stresses until the tissues are regenerated. We further employed the deformation recovery ratio to compare the flexibleness of the wet scaffold samples. The deformation recovery ratio of the composite sponges is in the range of 87.4–91.5%, suggesting the good elasticity of the samples. The decreased deformation recovery ratio of the composite scaffold at relatively high CNCs loading (200%) is attributed to both the decrease in the CS content of the scaffolds and the increase in the scaffold density.

3.3. *Morphology and crystal structure of the CS/CNCs composite scaffolds*

The pore size of tissue engineering scaffolds affects cell adhesion, proliferation, and differentiation. The scaffold pore size must be small enough to ensure mechanical integrity, but large enough to cell growth and the nutrient diffusion (Hollister, 2005). Stereoscopic microscope analysis was performed to analysis the 3D architecture of the prepared scaffolds. Fig. 3 shows the microscope micrographs with different magnification of the scaffolds. All the scaffolds exhibit a uniform porous structure at different angles and depths. Both the CS and CS/CNCs composite scaffolds are highly porous and interconnected with a pore size of 200 ± 40 μm. The pore shape and size of the composite scaffolds are similar to the pure CS scaffolds even when the CNCs loading is as high as 200%. So the addition of CNCs has slight effect on the formation of porous structure of the CS scaffold. However, the strength of the composite scaffolds increases with CNCs as illustrated in the compressive properties determination above.

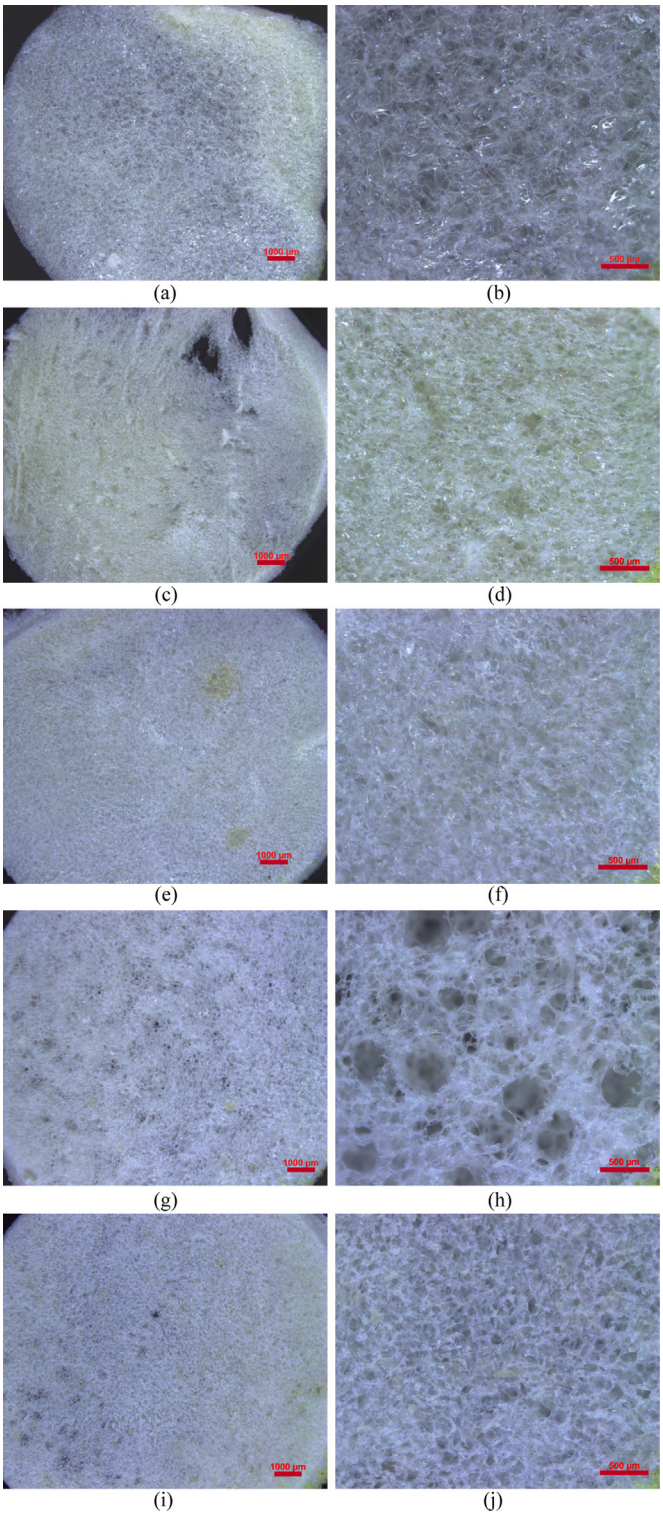

Fig. 3. Stereoscopic microscope micrographs of the chitosan/CNCs composite scaffolds: (a, b) chitosan; (c, d) 20%; (e, f) 50%; (g, h) 100%; (i, j) 200%.

The cross-sections of the scaffolds were further observed by SEM (Fig. 4). The pure CS scaffold have a highly porous structure with interconnected pores with diameter in the range of 100–200 μm. The CS/CNCs composite scaffolds also show regular network structure with numerous pores with much bigger dimension as seen from the images at same magnification. This suggests that the ice crystal in the mixture solution is bigger than that in the pure CS solution. During freeze-drying process, the ice crystals

transfer into pore. No CNCs can be clearly identified in the pore wall of the composite scaffold, which can be due to the good interfacial compatibility of the CS/CNCs composites. The pore structure of the composites scaffold is expected to be benefit for the enhancement of the cell adhesion and growth.

Fig. 5 shows the XRD patterns of the different scaffolds and the CNCs. CS scaffold has a main crystalline peak at around $2\theta = 23^\circ$ and an amorphous hump at around $2\theta = 10^\circ$ (Yang et al., 2012). CNCs exhibit two strong scattering peaks at around 2θ of 9.6° (020 plane) and 19.5° (110 plane) and three other weak peaks at 21° (120 plane), 23° (130 plane) and 26° (013 plane) (Goodrich & Winter, 2007). The CS/CNCs composite also shows the diffraction peaks similar with the CNCs, suggesting that the crystal structure of CNCs in the composite is not changed. With the increase in the CNCs loading, the diffraction peaks intensity increase. However, when CNCs loading is as high as 200%, the peak intensity slightly decreases. This may be due to that CNCs aggregate in the composite scaffold at relatively high loading. In total, from the stereoscopic microscope, SEM and XRD results, CNCs can be well distributed in the composite scaffolds with no significant effect on the pore structure.

3.4. Porosity and water absorption ratio of the CS/CNCs composite scaffolds

To further illustrate the influence of CNCs on the physical and chemical properties of CS scaffold, the density, porosity, and water uptake ratio were analyzed (Fig. 6). The density of the sample ranges from 0.030 to 0.068 g/cm^3. These ultra-low density materials are produced by replacement of water with air during the freeze-drying process. Pure CS scaffold exhibits the lowest density among the samples. The density of the composite scaffolds is linearly increases with CNCs loading. When the loading of CNCs is 200%, the density of the composite scaffold is about twice of that of the pure CS scaffold. The increased density of composite scaffolds is attributed to the

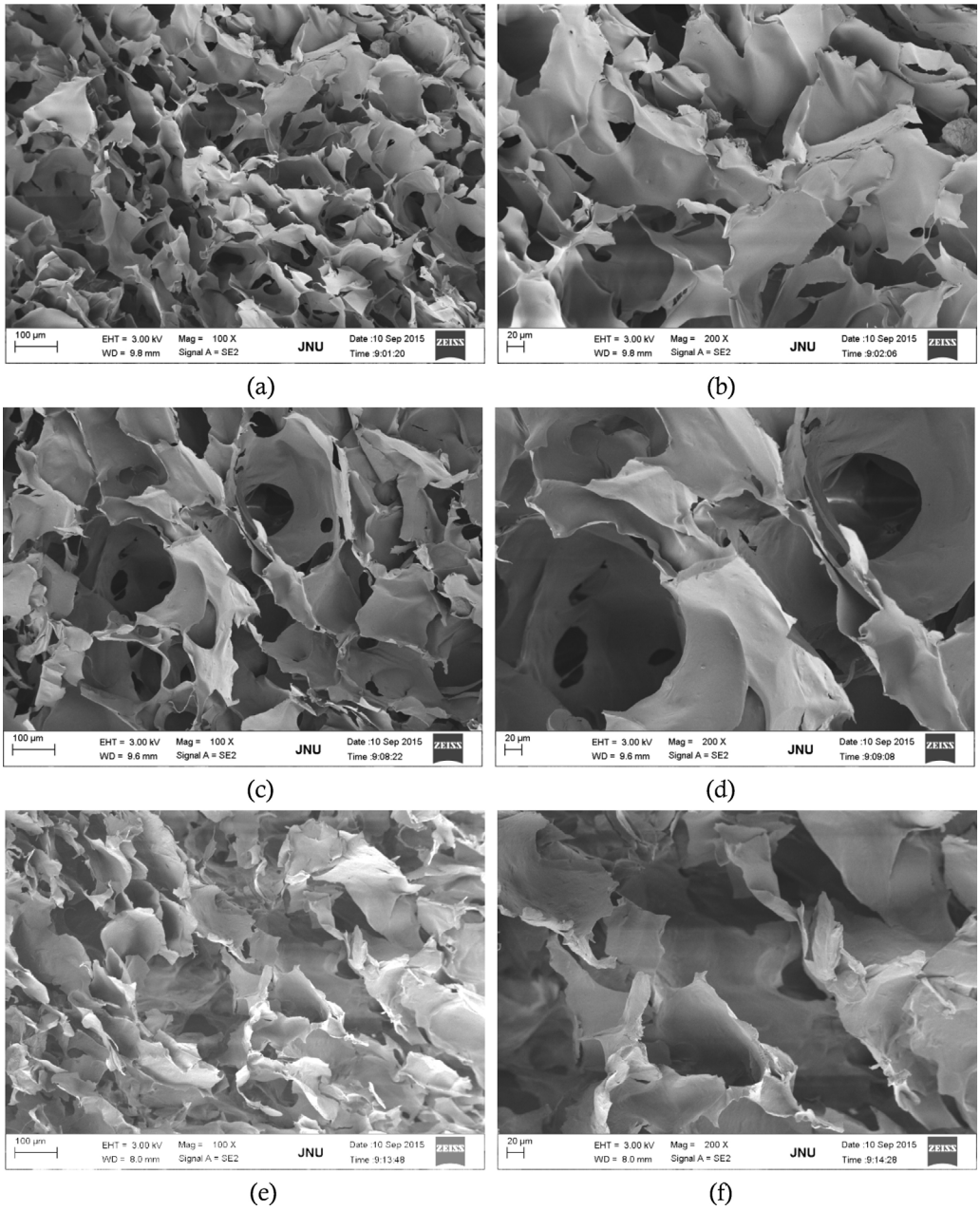

Fig. 4. SEM photos of chitosan/CNCs composite scaffolds with different magnification: chitosan (a b); 20% (c d); 50% (e f); 100% (g h); 200% (i j).

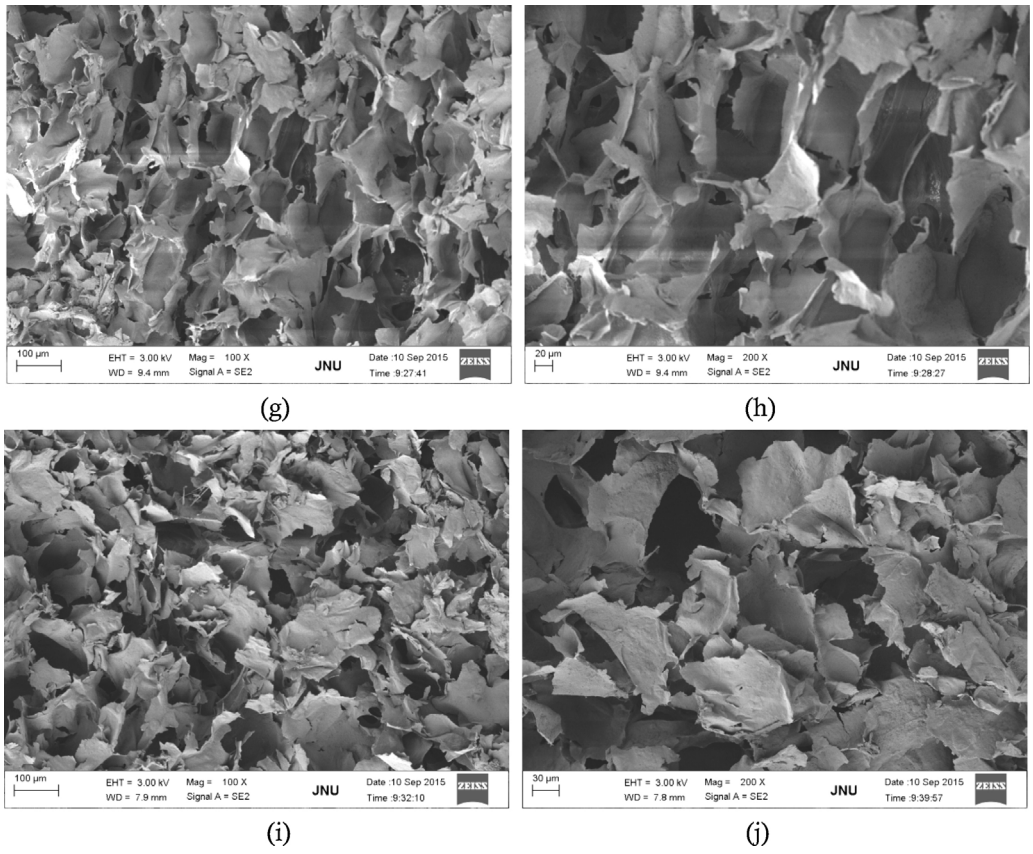

Fig. 4. (*Continued*)

greater material content in scaffold, as we fixed the water volume during the preparation of the scaffolds. The increased density of the composite scaffold contributes to the increased compressive performance.

High porosity of scaffold is critical factor in tissue repairing and regeneration, as the cell and nutrients can freely move. The pure CS scaffolds show porosity of 80.1%. The porosity (84.0%) of composite scaffold with 20% CNCs loading is maximum among the samples. By further loading of CNCs, the porosity of the scaffold slightly decreases, which is also attributed to the higher material content in the composite scaffolds. Incorporation of nanoparticles into CS always leads to slightly decreased porosity of the scaffold (Liu, Dai, Shi, Xiong & Zhou, 2015; Venkatesan, Qian, Ryu, Ashok Kumar & Kim, 2011).

Water uptake experiment of scaffolds was determined to illustrate the influence of CNCs on the absorption of physiological fluid of the scaffolds. All the scaffolds show water uptake ratio in the range of 91.3–96.8%. The addition of small amount CNCs to CS nearly has no effect on the water uptake ratio of the scaffold. This may due to that both CS and CNCs are hydrophilic, they can absorb water after immersing the scaffold in water. However, when the loading of CNCs is as high as 200%, the water uptake ratio is 91.3% which is slightly lower than the other groups. In total, the density, porosity and water absorption of CS/CNCs composite scaffolds can satisfy the requirement of tissue engineering and be tailored via the change of the loading of CNCs.

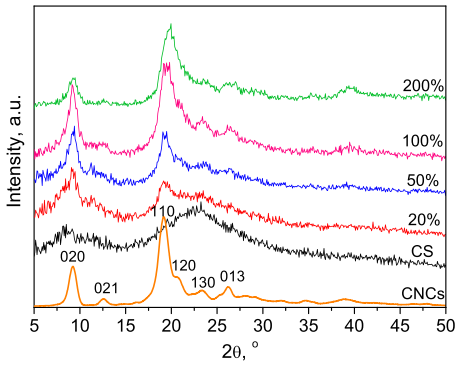

Fig. 5. XRD patterns for chitosan/CNCs composite scaffolds.

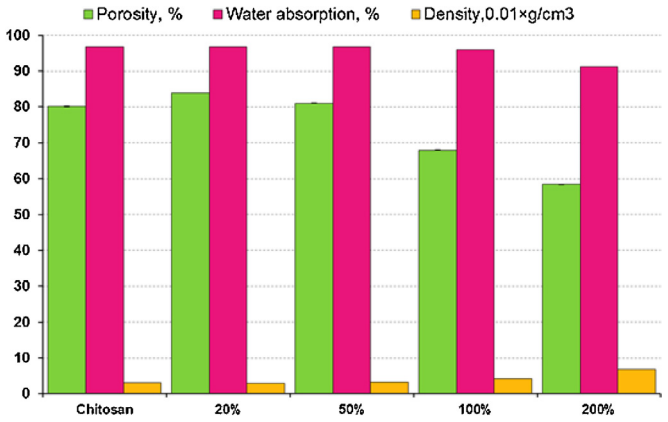

Fig. 6. Density, porosity, water absorption of chitosan-CNCs composite scaffolds.

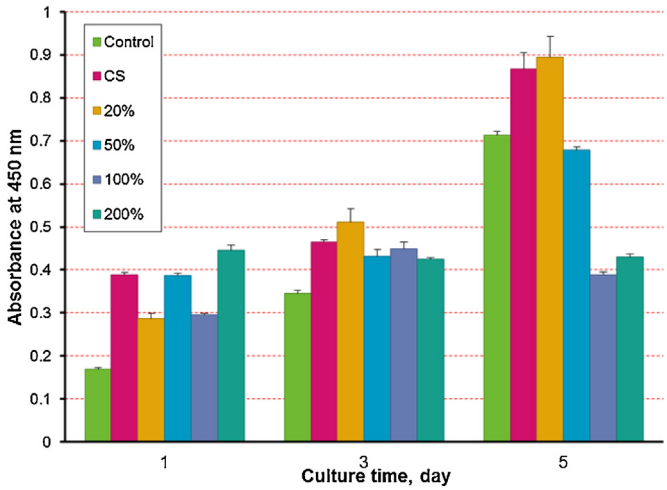

Fig. 7. CCK-8 viability assay of MC3T3-E1 cells after 1, 3, and 5 day cell culture on neat CS and CS/CNCS composite scaffolds in comparison with control group (TCPS) ($n = 4$).

3.5. Cell adhesion and proliferation on pure CS and CS/CNCs composites

The cytotoxicity of the scaffolds was firstly assessed by CCK-8 method using MC3T3-E1 cells line, and the results are summarized in Fig. 7. Compared with the control groups (TCPS), all the materials can support cell growth well after 1 day and 3 day culture. This indicates that both CS and CS/CNCs composite scaffolds exhibit good cytocompatibility. Also, the cell growth increases continually with the culture time for all the groups (expect the composites with 200% CNCs loading group), as the absorbance increase with the culture time. MC3T3-E1 cell population is comparable on the composite scaffolds with the pure CS after 1, 3, 5 days of culture. The cell viability of the cells on the composite scaffold with relatively low CNCs content (20% CNCs) is increased after 3 day and 5 day culture, which may due to the increase of the surface roughness by the incorporation of CNCs (Thein-Han & Misra, 2009). The increased viable cells number suggests the low cytotoxicity of CNCs at a certain amount. The large amount addition of CNCs with long culture time can induce decrease in cell viability, which is attributed to the lack of nutrition due to the dissolution of the materials with high CNCs loading in the cell culture medium.

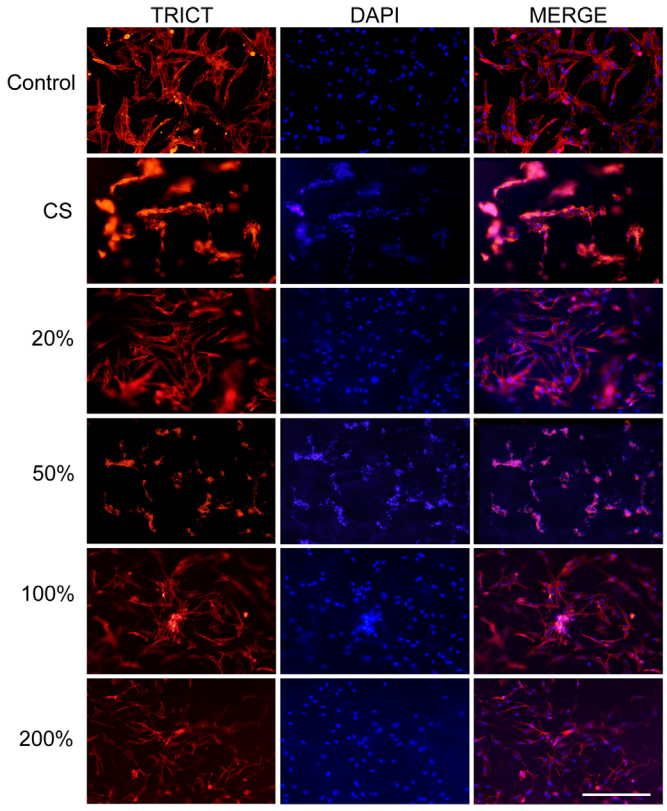

Fig. 8. Fluorescence microscope images of the CS/CNCs composite scaffolds for osteoblast (scale bar is 400 μm).

The morphology of the preosteoblast MC3T3-E1 on the materials was further studied using fluorescence microscope. DAPI stained nuclei and phalloidin-TRITC stained skeleton fluorescent images of these cells on different materials are shown in Fig. 8. Consistent with the cell viability result, it is clearly seen that the cells number increases for the composite samples compared with the pure CS. A good cell distribution and penetration throughout the 3D porous scaffold are evident from the fluorescence microscopic images. The cells appear to attach mainly around the pore walls and the pores are filled with cells. The cells are present individually or as aggregates on the scaffolds. The pores of the scaffolds are large for cell growth. Therefore, from fluorescence microscopy the proliferation of osteoblasts on the CS/CNCs scaffolds is greater in relation to pure CS scaffolds, suggesting their better cytocompatibility. Due to that the cells in the materials are located in different depth of the 3D scaffolds, it is hard to focus all the cells in a sample. It is also suggested that incorporation of CNCs enhances the attachment and proliferation of cells on the composite, as the cells on the composite scaffolds exhibit a well spread morphology after the same period of incubation. The enhanced attachment and proliferation is due to the good biocompatibility of CNCs and the increase in the surface roughness of the composites. The low cytotoxicity and good biosafety of CNCs in other polymer composite systems were also found in previous studies (Huang et al., 2015; Liu et al., 2016).

4. Conclusions

Chitin nanocrystals with length and width of 300 and 20 nm were mixed with CS aqueous solution. CS/CNCs composite scaffolds prepared by freeze-drying exhibited significant enhancement in compressive strength and modulus compared with pure CS scaffold both in dry and wet state. A well-interconnected porous structure with size of ~200 μm and over 80% porosity were found in the composite scaffolds. The crystal structure of CNCs was retained in the composite scaffolds. The incorporation of CNCs leaded to increase in the scaffold density. The CNCs nearly had no effect on the water uptake ratio of the scaffold. Moreover, the composite scaffolds were successfully applied as scaffolds for MC3T3-E1 osteoblast cells, showing their excellent biocompatibility and low cytotoxicity. The results of fluorescent micrographs images revealed that CNCs markedly promoted the cell adhesion and proliferation of the osteoblast cells on CS. The biocompatible composite scaffolds with enhanced mechanical properties have potential application in bone tissue engineering.

Acknowledgements

This work was financially supported by National High Technology Research and Development Program of China (2015AA020915), the National Natural Science Foundation of China (grant No. 51473069 and 51502113), and the Guangdong Natural Science Funds for Distinguished Young Scholar (grant No. S2013050014606), Science and Technology Planning Project of Guangdong Province (2014A020217006), Guangdong

Special support program (2014TQ01C127), the Special Fund for Ocean-Scientific Research in the public interest (201405105), and the Fundamental Research Funds for the Central Universities (21615204).

Appendix A. Supplementary data

Supplementary data associated with this article can be found, in the online version, at http://dx.doi.org/10.1016/j.carbpol.2016.07.042.

References

Capadona, J. R., Shanmuganathan, K., Tyler, D. J., Rowan, S. J., & Weder, C. (2008). Stimuli-responsive polymer nanocomposites inspired by the sea cucumber dermis. *Science*, *319*(5868), 1370–1374.

Carter, D. R., & Hayes, W. C. (1976). Bone compressive strength: The influence of density and strain rate. *Science*, *194*(4270), 1174–1176.

de Mesquita, J. P., Donnici, C. L., & Pereira, F. V. (2010). Biobased nanocomposites from layer-by-layer assembly of cellulose nanowhiskers with chitosan. *Biomacromolecules*, *11*(2), 473–480.

Ding, F., Deng, H., Du, Y., Shi, X., & Wang, Q. (2014). Emerging chitin and chitosan nanofibrous materials for biomedical applications. *Nanoscale*, *6*(16), 9477–9493.

Fan, H., Wang, L., Zhao, K., Li, N., Shi, Z., Ge, Z., et al. (2010). Fabrication, mechanical properties, and biocompatibility of graphene-reinforced chitosan composites. *Biomacromolecules*, *11*(9), 2345–2351.

Goodrich, J. D., & Winter, W. T. (2007). α-Chitin nanocrystals prepared from shrimp shells and their specific surface area measurement. *Biomacromolecules*, *8*(1), 252–257.

Gopalan Nair, K., & Dufresne, A. (2003). Crab shell chitin whisker reinforced natural rubber nanocomposites. 1. Processing and swelling behavior. *Biomacromolecules*, *4*(3), 657–665.

Hollister, S. J. (2005). Porous scaffold design for tissue engineering. *Nature Materials*, *4*(7), 518–524.

Huang, Y., Zhang, L., Yang, J., Zhang, X., & Xu, M. (2013). Structure and properties of cellulose films reinforced by chitin whiskers. *Macromolecular Materials and Engineering*, *298*(3), 303–310.

Huang, Y., Yao, M., Zheng, X., Liang, X., Su, X., Zhang, Y., et al. (2015). Effects of chitin whiskers on physical properties and osteoblast culture of alginate based nanocomposite hydrogels. *Biomacromolecules*, *16*(11), 3499–3507.

Justin, R., & Chen, B. (2014). Characterisation and drug release performance of biodegradable chitosan-graphene oxide nanocomposites. *Carbohydrate Polymers*, *103*, 70–80.

Lau, C., Cooney, M. J., & Atanassov, P. (2008). Conductive macroporous composite chitosan- carbon nanotube scaffolds. *Langmuir*, *24*(13), 7004–7010.

Li, Q., Zhou, J., & Zhang, L. (2009). Structure and properties of the nanocomposite films of chitosan reinforced with cellulose whiskers. *Journal of Polymer Science Part B: Polymer Physics*, *47*(11), 1069–1077.

Lin, N., Huang, J., & Dufresne, A. (2012). Preparation, properties and applications of polysaccharide nanocrystals in advanced functional nanomaterials: A review. *Nanoscale*, *4*(11), 3274–3294.

Liu, M., Wu, C., Jiao, Y., Xiong, S., & Zhou, C. (2013). Chitosan-halloysite nanotubes nanocomposite scaffolds for tissue engineering. *Journal of Materials Chemistry B*, *1*(15), 2078–2089.

Liu, M., Dai, L., Shi, H., Xiong, S., & Zhou, C. (2015). In vitro evaluation of alginate/halloysite nanotube composite scaffolds for tissue engineering. *Materials Science and Engineering: C*, *49*, 700–712.

Liu, M., Huang, J., Luo, B., & Zhou, C. (2015). Tough and highly stretchable polyacrylamide nanocomposite hydrogels with chitin nanocrystals. *International Journal of Biological Macromolecules*, *78*, 23–31.

Liu, M., Peng, Q., Luo, B., & Zhou, C. (2015). The improvement of mechanical performance and water-response of carboxylated SBR by chitin nanocrystals. *European Polymer Journal*, *68*, 190–206.

Liu, H., Liu, W., Luo, B., Wen, W., Liu, M., Wang, X., et al. (2016). Electrospun composite nanofiber membrane of poly (L-lactide) and surface grafted chitin whiskers: Fabrication, mechanical properties and cytocompatibility. *Carbohydrate Polymers*, *147*, 216–225.

Lu, Y., Sun, Q., She, X., Xia, Y., Liu, Y., Li, J., et al. (2013). Fabrication and characterisation of α-chitin nanofibers and highly transparent chitin films by pulsed ultrasonication. *Carbohydrate Polymers*, *98*(2), 1497–1504.

Pawlak, A., & Mucha, M. (2003). Thermogravimetric and FTIR studies of chitosan blends. *Thermochimica Acta*, *396*(1), 153–166.

Sriupayo, J., Supaphol, P., Blackwell, J., & Rujiravanit, R. (2005a). Preparation and characterization of α-chitin whisker-reinforced chitosan nanocomposite films with or without heat treatment. *Carbohydrate Polymers*, *62*(2), 130–136.

Sriupayo, J., Supaphol, P., Blackwell, J., & Rujiravanit, R. (2005b). Preparation and characterization of α-chitin whisker-reinforced poly(vinyl alcohol) nanocomposite films with or without heat treatment. *Polymer*, *46*(15), 5637–5644.

Suh, J.-K. F., & Matthew, H. W. (2000). Application of chitosan-based polysaccharide biomaterials in cartilage tissue engineering: A review. *Biomaterials*, *21*(24), 2589–2598.

Sweetman, L. J., Moulton, S. E., & Wallace, G. G. (2008). Characterisation of porous freeze dried conducting carbon nanotube-chitosan scaffolds. *Journal of Materials Chemistry*, *18*(44), 5417–5422.

Tang, C., Xiang, L., Su, J., Wang, K., Yang, C., Zhang, Q., et al. (2008). Largely improved tensile properties of chitosan film via unique synergistic reinforcing effect of carbon nanotube and clay. *The Journal of Physical Chemistry B*, *112*(13), 3876–3881.

Thein-Han, W. W., & Misra, R. D. K. (2009). Biomimetic chitosan-nanohydroxyapatite composite scaffolds for bone tissue engineering. *Acta Biomaterialia*, *5*(4), 1182–1197.

Venkatesan, J., Qian, Z.-J., Ryu, B., Ashok Kumar, N., & Kim, S.-K. (2011). Preparation and characterization of carbon nanotube-grafted-chitosan-natural hydroxyapatite composite for bone tissue engineering. *Carbohydrate Polymers*, *83*(2), 569–577.

Wang, X., Du, Y., Luo, J., Lin, B., & Kennedy, J. F. (2007). Chitosan/organic rectorite nanocomposite films: Structure, characteristic and drug delivery behaviour. *Carbohydrate Polymers*, *69*(1), 41–49.

Wongpanit, P., Sanchavanakit, N., Pavasant, P., Bunaprasert, T., Tabata, Y., & Rujiravanit, R. (2007). Preparation and characterization of chitin whisker-reinforced silk fibroin nanocomposite sponges. *European Polymer Journal*, *43*(10), 4123–4135.

Yang, Y., Cui, J., Zheng, M., Hu, C., Tan, S., Xiao, Y., et al. (2012). One-step synthesis of amino-functionalized fluorescent carbon nanoparticles by hydrothermal carbonization of chitosan. *Chemical Communications*, *48*(3), 380–382.

Zhang, Y., & Zhang, M. (2001). Synthesis and characterization of macroporous chitosan/calcium phosphate composite scaffolds for tissue engineering. *Journal of Biomedical Materials Research*, *55*(3), 304–312.